



UAV video-based estimates of nearshore bathymetry[☆]

Athina M.Z. Lange^{*}, Julia W. Fiedler, Mark A. Merrifield, R.T. Guza

Scripps Institution of Oceanography, La Jolla, CA, USA

ARTICLE INFO

Keywords:

Bathymetry
Remote sensing
Machine learning
UAV

ABSTRACT

Nearshore bathymetry estimated from video acquired by a hovering UAV is compared with ground truth. Bathymetry estimates from the widely used cBathy algorithm are improved by crest tracking (with machine learning-aided annotations) from near breaking through the surf zone. Individual wave crests (distinguished from the breaking wave toe that can move down the wave front face) in video timestacks are determined with a deep-learning neural network and surf zone depth estimates are computed from the wave celerity. Time-2D spatial transforms (cBathy) are used to estimate wave celerity and depth between the surf zone and 10m depth. Composite profiles (cBathyCT), formed by joining cBathy and crest-tracking solutions near the surf zone seaward edge, based on a newly determined $\gamma(x)$ parameter, avoid the large cBathy errors associated with the onset of breaking. Including an additional topography survey for the foreshore region, provides full nearshore bathymetry profiles. Incident wave heights were relatively constant on each day but varied over days between 0.55 - 2.15m. Averaged over all 17-minute hovers and cross-shore transects (112 total), surf zone depths errors were relatively small (average root-mean-square error (RMSE) = 0.17m, (Bias) = 0.06m) after including a heuristic nonlinear correction to the linear phase speed. Between the seaward surf zone edge and 10m depth, errors are similar to previous cBathy studies: (RMSE) = 0.87m, (Bias) = 0.58m with the largest errors in deepest water. Beach profiles were generally similar for all 8 test days, concave up with a slight terrace (no sandbar) and small alongshore depth variations. Accuracy was lower on one transect with a shallow reef.

1. Introduction

Accurate bathymetry is critical to understanding nearshore processes like beach erosion and accretion, the fate of beach nourishment sand, sandbar migration, and the corresponding hydrodynamics. While topography above the waterline may be monitored efficiently with mobile scanning LiDAR or photogrammetry, subaqueous nearshore bathymetry is usually less well-known owing to the expense of in situ subaqueous surveys. Early-warning overtopping forecasts can therefore have limited accuracy owing to over-simplified (planar) or outdated bathymetry (Stephens and Cloke, 2014; Stokes et al., 2019; Jordi et al., 2019; Stokes et al., 2021; Merrifield et al., 2021; USGS, 2022; Gomes da Silva et al., 2020, and references therein).

Remote sensing via satellite or video can provide relatively wide-area, low-cost observations of nearshore bathymetry. Satellite subaqueous observations require relatively clear water, and resolution in space and time can be limited (Vanderstraete et al., 2003; Mallet and Bretar, 2009; Jing and Datt, 2010; Abileah and Trizna, 2010; Gao, 2009; Zuckerman and Anderson, 2018; Legleiter and Harrison, 2019; Li et al., 2019; Geyman and Maloof, 2019). Enabled by improved cameras

and computing power, nearshore bathymetry can be estimated using video observations of surface wave dissipation and celerity (Holman and Haller, 2013). Wave dissipation methods use high-intensity peaks in time-averaged images (timex e.g. ARGUS stations (5-camera system, Holman and Stanley, 2007)) to identify persistent foam caused by depth-limited breaking on sandbar crests (Lippmann and Holman, 1989; Aarninkhof, 2005; Collins et al., 2020). Celerity-based methods exploit the dependence of wave celerity on depth (Stockdon and Holman, 2000; Plant et al., 2009; Holman et al., 2013; Rutten et al., 2017; Radermacher et al., 2014; Holman and Haller, 2013; Wengrove et al., 2013; Bergsma et al., 2016; Catálan and Haller, 2008; Almar et al., 2009; Thuan et al., 2019; Tsukada et al., 2020).

The accuracy of estimated depths can be improved with prior imagery from long-term observations and sophisticated numerical modeling. Observed and numerical model predictions of wave dissipation patterns can be coupled and used in data-assimilation schemes that estimate depth from pixel intensity, wave celerity and other observables (Aarninkhof, 2005; van Dongeren et al., 2008). Full end-to-end machine learning methods combine image analysis with extensive past

[☆] This document is the results of the research project funded by the U.S. Army Corps of Engineers and the California Department of Parks and Recreation.

^{*} Corresponding author.

E-mail address: alange@ucsd.edu (A.M.Z. Lange).

bathymetry observations and sophisticated wave modeling (Collins et al., 2020).

Bathymetry is often required in areas lacking continuous, long-term observations, and the fixed, elevated platform for a permanent camera system. To address this, hovering UAVs (Uncrewed Aerial Vehicles) have increasingly been used for nearshore observations (Brodie et al., 2019). In this study, we evaluate the accuracy of bathymetry estimates obtained from relatively short (17-minute) observations taken from a hovering UAV, without use of prior imagery, bathymetry surveys, or numerical wave models. We use celerity and the proportion of waves breaking in relation to cross-shore location to refine depth estimates in the outer surf zone, where the mix of both broken and unbroken creates errors in existing methods.

Bathymetry is estimated in four steps: (1) cBathy is applied offshore of the surf zone, (2) timestack images are used to track individual wave crests and locate the onset of breaking. Crests are tracked with a deep learning U-Net algorithm, (3) surf zone depth is estimated using the observed crest celerity and shallow water theory with a simple nonlinear correction and (4) full depth profiles (from backbeach to 8m depth) combine cBathy offshore, crest tracking in the surf zone, and a low-tide survey of the subaerial beach.

In Section 2, existing video-based estimates of bathymetry are reviewed and extended. Observations are described in Section 3. In Section 4, methods valid within and seaward of the surf zone are combined, yielding composite profiles that are then compared with ground truth bathymetric surveys. Error sources and the need for additional model development to include complex bathymetry are discussed in Section 5.

2. Background

2.1. cBathy

cBathy (Holman et al., 2013; Holman and Bergsma, 2021) is a popular, open-source celerity-based depth inversion algorithm. It fits the most coherent frequency–wavenumber pairs (default of 4) to the cross-spectra of all pixels within a given area around a point. The depth estimates are based on the nonlinear best fit from the dominant frequency–wavenumber pairs from the surrounding points and the linear dispersion relationship (see Table 2 for cBathy parameters used here). cBathy (RMSE) (average root-mean-square-error) of individual estimates from stationary platforms for cBathy v2.0 are $\sim 0.56\text{m}$ (Holman and Bergsma, 2021) and for v1.2 have varied between 0.51 and 2.05m (Table 1, Brodie et al., 2018), insitu validation is limited to $< 7\text{m}$ depth at the Field Research Facility (FRF) in Duck, NC, USA, and reasonably good agreement ($\langle \text{RMSE} \rangle = 0.56\text{m}$, $\langle \text{Bias} \rangle = -0.41\text{m}$) between cBathy v1.0 and observations as deep as 14m were obtained at Agate Beach, Oregon, USA using an elevated (128m) headland-mounted camera (Holman et al., 2013). The offshore extent of accurate cBathy depends on camera quality, elevation, and stabilization (Bergsma et al., 2019). This is particularly important for UAV's, where cBathy (RMSE) can be $\sim 2.35\text{m}$ (Bergsma et al., 2019). Results here extend to 10m depth, about 500m from the backbeach.

cBathy assumes spatially homogeneous waves and bathymetry over a given tile (cBathy v2.0 uses an adaptive tile size). Prior to wave breaking, wave front faces usually appear darker than wave rear faces. However, when waves begin breaking, the foam-dominated front wave face becomes much brighter (whiter) than the back face, reversing the pattern from offshore. Switching between dark and light wave faces within a tile can cause large celerity and depth overestimates and is known as the Modulation Transfer Function (MTF). Holman et al. (2013) suggests using the shifting cross-shore location of the “switching region” over a tidal cycle (or longer) and a Kalman filter to reduce these errors. Kalman results accumulate over a series of prior data collections, with each new run improving the estimate until the results stabilize after roughly one or two days (Holman and Bergsma, 2021).

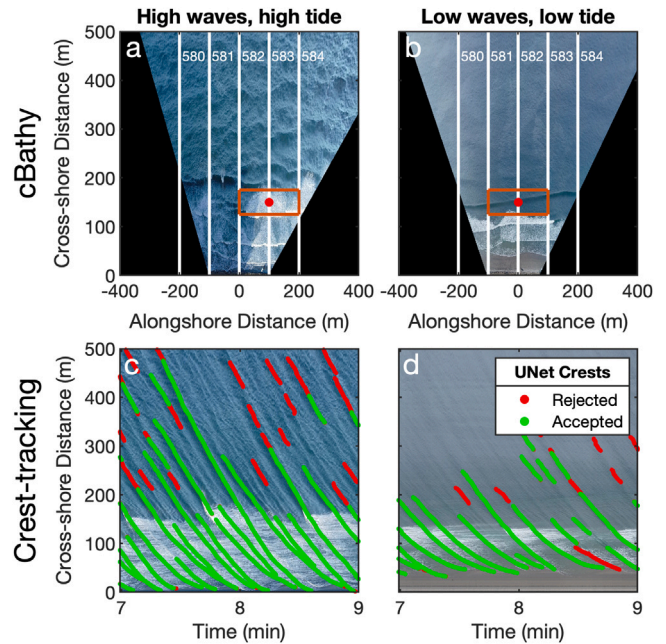


Fig. 1. Contrasting conditions (left) Dec 15th, 2021, relatively high waves and high tide ($H_s = 1.96\text{m}$, tide = 1.41m) and (right) Dec 2nd, 2021, lower waves and lower tide ($H_s = 0.64\text{m}$, tide = 0.46m). Beach is at the bottom of each image. (Top) Orthorectified planview images of shoaling region and surf zone. Orange rectangle encloses a potential tile of 200m-alongshore by 50m-cross-shore area used for each cBathy depth estimate (red dot). Box dimensions increase offshore. Ground-truth survey cross-shore transects (white) are identified by “MOP” number. (Bottom) wave crest trajectories (cross-shore location versus time) determined by a deep learning algorithm on MOPs (c) 583 and (d) 582. Red trajectories were rejected for further analysis.

Alternatively, Bergsma et al. (2019) used the absolute value of the pixel intensity time derivative to augment timestacks and reduce foam on the image. This modified signal is included in the input data for cBathy and reduces the surf zone $\langle \text{RMSE} \rangle$ from 3.1m to 1.3m. Here, surf zone depths are inferred from 17-minute timestacks of individual waves (Fig. 1 c,d), without Kalman filtering.

2.2. Timestack analysis

Timestack images (Fig. 1 c,d) show wave evolution over time on a single cross-shore transect, rather than snapshots of a 2D field (Fig. 1 a,b). The x-location of individual shoaling and breaking waves can be determined in sequential pixel columns. Depth estimates based on video celerity are necessarily heuristic. The relationship between pixel intensity and sea surface elevation is a required assumption (Lippmann and Holman, 1991). Many RGB image-based timestack analyses use standard edge detection algorithms (Canny or Sobel, Szeliski, 2022) to identify the wave toe, the bright front edge of the incoming, breaking waves that sharply contrast with the darker water in front. However, as spilling breaking begins and the roller slides down the wave face, the toe moves faster than the crest, increasing the estimated speed and complicating depth inversions. The roller toe eventually reaches a relatively stable position on the wave face, and in the inner surf zone is a stable proxy for the wave crest (Stive, 1980; Basco, 1985; Svendsen et al., 2003). Traditional computer vision approaches have difficulty detecting wave crests (as opposed to toes) robustly inside the surf zone due to the complexity of foam patterns (Stringari et al., 2019). Yoo et al. (2011) combined Radon-transform edge tracking and a nonlinear wave propagation model to estimate shallow water ($h < 2\text{m}$) bathymetry accurately ($\langle \text{RMSE} \rangle = 0.25\text{m}$, $\langle \text{Bias} \rangle = 0.1\text{m}$) with relatively low incident wave heights ($H_s < 0.8\text{m}$) on bathymetry not dissimilar to Torrey Pines State Beach, CA, USA (our primary study

site). Stringari et al. (2019) estimates phase speed using a combination of Sobel edge detection, pixel-intensity extrema, and machine learning to extract the white signature of ‘foam corresponding to the crests of breaking waves’ with surf zone wave heights and depths less than 1m.

We were unable to implement (Stringari et al., 2019), Yoo et al. (2011), and Bergsma et al. (2019) with the present observations. Almar et al. (2009) and Tsukada et al. (2020) obtain mean wave celerity using a cross-correlation technique with varying space and time intervals. However, for a test case, the correlation methods were relatively noisy for the present data and still exhibit the well-known errors in the break-point transition zone (not shown). Here we describe an alternative and reproducible crest-tracking algorithm with good surf zone performance, available in a [GitHub repository](#). A crest-tracking algorithm with good surf zone performance with H_s as large as 2m in 4m depth is described and combined with cBathy estimates valid offshore and a low-tide subaerial survey to obtain a full nearshore profile.

2.3. Surf zone wave celerity

In linear (small amplitude) shallow water theory waves advance with celerity

$$c = \sqrt{gh}. \quad (1)$$

However, nonlinear shoaling and breaking waves travel with amplitude-dependent phase speeds faster than c (Svendsen and Buhr Hansen, 1976; Svendsen et al., 2003). For idealized cnoidal and solitary waves with wave height H

$$c^2 = g(h + H) = gh(1 + H/h), \quad (2)$$

(Inman et al., 1971; Thornton and Guza, 1982; Stockdon and Holman, 2000). Assuming a saturated surf zone with $\gamma = H_{rms}/h$ yields

$$h_{estimate} = c^2 / (g(1 + \gamma)). \quad (3)$$

Surf zone waves are not constant shape as assumed in (2). Although phase speeds for nonlinear random waves generally increase with increasing amplitude, (3) is a heuristic simplification.

Variations in observed γ between 0.3 and 1.1 have been ascribed to the effects of beach slope, breaker wave type (e.g. plunging versus spilling) and location within the surf zone (Raubenheimer et al., 1996; Catálan and Haller, 2008; Brodie et al., 2018). For both broken and unbroken waves, c on average increases with increasing amplitude and depth but celerity observed on a wave-by-wave basis diverges from Eq. (3). Despite these complications, corrections based on Eq. (3) consistently improve celerity-based surf zone depth estimates (Holland, 2001; Svendsen et al., 2003; Catálan and Haller, 2008; Yoo et al., 2011; Tissier et al., 2015; Fiedler et al., 2021; Martins et al., 2018). We compare observed depths with estimates from linear (Eq. (1)) and simplified nonlinear (Eq. (3)) crest-tracking methods.

3. Observations

We completed 52 UAV hovers in San Diego, California with a DJI Phantom 4 RTK drone: 39 hovers over 6 days at Torrey Pines State Beach (July 2020–Dec 2021), 6 hovers during 1 day at Cardiff State Beach, and 7 hovers over 1 day at Scripps Institution of Oceanography (SIO). Wave conditions were relatively constant during data collection on each day, and varied over the 8 days, with $0.55 < H_s < 2.15$ m and $9 < T_p < 17.6$ s (Table 1). Transects are defined by MOnitoring and Prediction (MOP) System number (O'Reilly et al., 2016). Torrey Pines depth varies little alongshore with a maximum difference of approximately 1m across 300 – 500m (Fig. 2 a insert). Bathymetries at the three sites are similar, with the exception of a pronounced bedrock reef on MOP 667 at Cardiff and a well-developed terrace at SIO (Fig. 2). The beach profile near and above the waterline was measured with subaerial (LiDAR or photogrammetry) beach surveys on the same day as UAV hovers.

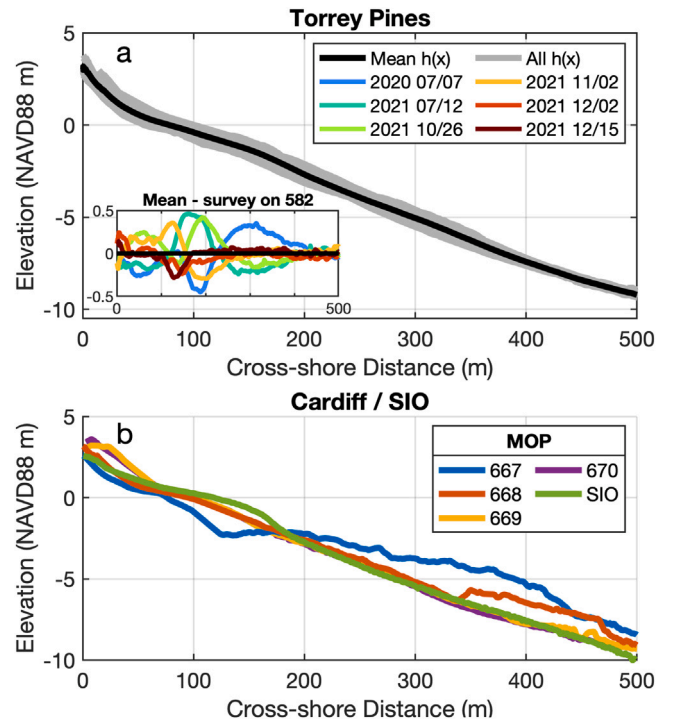


Fig. 2. Seabed elevation versus cross-shore distance at (a) Torrey Pines. Mean of all transects and days (bold, $n = 42$) and shaded by range of all observed profiles. (insert) Deviations of MOP 582 transect from mean, colored by date. (b) Cardiff (reef at $x > 125$ m on MOP 667, blue) and SIO (green MOP 514).

UAV hovers were typically ~ 17 -minutes (minimum 10-minutes). The UAV hovered between 27 and 91.5 m above NAVD88, with no significant difference in performance with height. JPEG images were extracted from the video using the ffmpeg tool at 10 Hz. RTK-surveyed, 1m x 1m checkerboards provide stability control points used for rectification with CIRN UAV Rectification software (Bruder and Brodie, 2020). Cross-shore timestacks were extracted at 20 m along-shore intervals, gridded up to 500m offshore at 0.1m spacing. The (dx, dt) size was kept constant across all extracted timestacks and is a trained part of the neural network.

Ground truth was insitu (labor-intensive) bathymetry surveys (jet ski, push dolly, All-Terrain Vehicle) on 100-m alongshore intervals to 10m depth usually obtained on the same day as the hovers, and always within one day. There were usually 3 cross-shore transects within the video field of view (Table 1), although the number varied with different video look angles. The 52 hovers included a total of 11 unique surveyed transects at 3 sites, with a total of 112 transects with ground truth.

4. Methods

Our proposed method combines an existing celerity-based depth inversion algorithm (cBathy v2.0, Holman et al., 2013; Holman and Bergsma, 2021), which has been shown to be most effective seaward of the surf zone, with nonlinear surf zone depth estimates derived from machine learning-aided timestack wave crest tracks. The method is implemented in four steps.

4.1. cBathy surf zone depth estimation

cBathy results based on a single hover (no Kalman filtering) have much larger RMSE in the surf zone than offshore, similar to Holman et al. (2013), Brodie et al. (2018), Bergsma et al. (2019) and others. Holman and Bergsma (2021) consider cBathy estimates unreliable when the cBathy 95% confidence interval $hErr > 0.5$. This criterion can

Table 1

UAV flight info and wave conditions from MOP forecasts in 10m depth. Incident wave parameters include significant wave height H_s , peak period T_p , and obliquity relative to beach normal.

Date	Location	Hovers (MOP transect)	H_s (m)	T_p (s)	Obliquity (degree)	Tide range (NAVD88 m)
Jul 07, 2020	Torrey Pines	13 (579 – 584)	0.89	11.3	–12	–0.27 – 1.13
Oct 10, 2020	Scripps	7 (513 – 514)	0.55	9	14	0.22 – 0.8
Jul 09, 2021	Cardiff	6 (670 – 667)	0.8	16.7	–21.5	0.28 – 0.9
Jul 12, 2021	Torrey Pines	6 (581 – 584)	0.7	10	7	–0.06 – 0.41
Oct 26, 2021	Torrey Pines	5 (581 583)	2.15	17.7	1	1.07 – 1.26
Nov 02, 2021	Torrey Pines	5 (581 583)	1.12	16.7	6	0.1 – 0.72
Dec 02, 2021	Torrey Pines	5 (581 583)	0.65	12.3	2	–0.22 – 0.49
Dec 15, 2021	Torrey Pines	5 (581 583)	1.96	15.4	–4	0.8 – 1.4

Table 2

cBathy v2.0 Parameters (Holman and Bergsma, 2021).

Parameter	Description	Value
Δt	Time series sampling interval	0.5 s
$(\Delta x_p, \Delta y_p)$	Pixel spacing	(5, 5) m
$(\Delta x_m, \Delta y_m)$	Analysis point spacing	(5, 25) m
h_{min}	Min acceptable depth	0.25 m
(L_x, L_y)	Analysis smoothing scale	(25, 100) m
κ	Smoothing scale expansion at outer boundary	3
f	Analysis frequency bins, range and df	[0.055 : 0.0005 : 0.25] Hz
N_{keep}	Number of frequency bins to retain	4

underestimate the width of the overpredicted data (Fig. 3 a) or fail to identify a narrow surf zone (Fig. 3 b) resulting in $\langle \text{RMSE} \rangle$ and $\langle \text{Bias} \rangle > 0.8\text{m}$. A constant threshold other than $\text{hErr} > 0.5$ did not reliably estimate where cBathy failed. An alternative criterion assumes that cBathy estimates are corrupted by a mix of breaking (white faced) and nonbreaking (dark faced) waves. The fraction of waves breaking (determined from timestacks, below) defines the region of cBathy validity as $> 95\%$ (inner surf zone) or $< 5\%$ (offshore) of waves breaking (Fig. 3 e,f), and can be used instead of the standard $\text{hErr} > 0.5$ as the region where cBathy fails. In addition, the fraction of wave breaking can also be used to determine a nonlinear correction (described in Section 4.3) to include in the cBathy estimates ($h_{\text{nonlinear}} = h_{\text{cBathy}} * \frac{1}{1 + \gamma_{\text{mean}}(x)}$). For all 3 error-filtered cBathy versions (only using $\text{hErr} < 0.5$, removing timestack derived wave-breaking region, and nonlinear correction to cBathy), estimates are interpolated across regions where cBathy fails (according to the different criteria, Fig. 3).

4.2. Deep learning for timestack-image wave crest detection

Traditional computer vision techniques, e.g. Canny or Sobel edge detection, often have difficulty accurately identifying the location of wave crests when foam is persistent (Stringari et al., 2019). Because manually identifying wave crests (e.g. through ground-truth annotations) can be time-consuming, we propose using a deep learning approach as an automated annotation tool (e.g. Collins et al., 2020). Our method is not intended to provide new information, but rather to aid in the tedious process of identifying wave crests, which we define as the location between the solid block of white water that is characteristic of a wave roller and the more interspersed longer tracks of foam on the back side of a broken wave (Appendix A Fig. 10 insert).

The training/validation dataset consists of 20 timestack-images with sparse (not for all waves) ground-truth provided by binary hand annotations of wave crests. To include a range of wave, lighting, and bathymetry conditions, one transect from each hover in Fall 2021 at Torrey Pines is included. Training used 16 randomly selected timestack-images and validation used 4. Note that because the deep learning approach is used here simply as an annotation tool, the specific choices of parameters of the neural network are of little importance.

Further details on the wave crest detection algorithm can be found in Appendix A. Fig. 10 shows the workflow for the crest-detection. An input timestack is provided and a binary output image of the detected

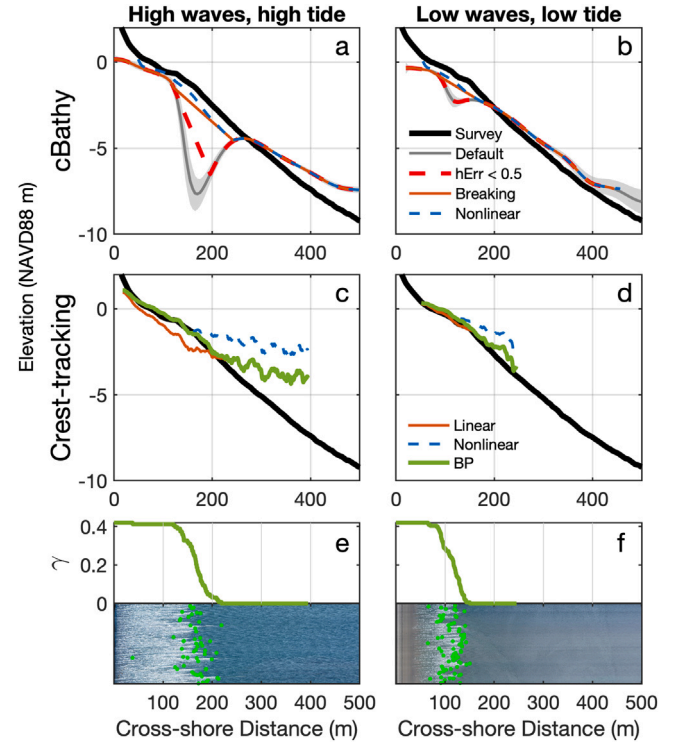


Fig. 3. Bed elevation versus cross-shore distance for relatively (a,c) high waves and tide, Dec 15th, 2021 ($H_s = 1.96\text{m}$, tide = 1.41m) and (b,d) low waves and tide, Dec 2nd 2021 ($H_s = 0.64\text{m}$, tide = 0.46m) at Torrey Pines State Beach, USA. Mean ground-truth survey (black). Remote sensing estimates: (a,b) cBathy: default (gray with hErr shaded), $\text{hErr} > 0.5\text{m}$ removed and interpolated over (red dashed), breaking region removed and interpolated (red solid) and (best cBathy-only method) with a nonlinear correction (blue dashed). (c,d) crest-tracking, linear (solid red), nonlinear (blue dashed), breakpoint transition (green). (e,f) effective $\gamma = H/h$ versus cross-shore distance above compressed view of the corresponding timestack with detected breakpoints shown (green dots). Effective $\gamma(x)$ is the mean of γ step functions for all waves in a given hover.

crests is returned. An example of the output wave crests superimposed on the timestack image can be seen in the insert.

4.3. Surf zone depth from crest-tracking

The surf zone method estimates the celerity of individual wave crests observed in timestacks using a deep learning neural network. Depth is recovered by inverting celerity using linear and nonlinear shallow water dispersion.

Crest tracks are extracted from U-Net binary output images (Fig. 10). The 2-D binary image is reduced to 1-pixel (0.1m, 0.1s) wide curves, and the (x, t) coordinates of the individual curves are detected by (1) finding the first offshore instance of the curve (where no other black points are found previously in time and further offshore in a given area), (2) following the crest, with the next coordinate detected by the shortest Euclidean distance between black points that follow in

time and are onshore of the current points, and (3) removing short curves (< 7.5 sec). Fig. 1 c,d shows the difference between the initial U-Net output and the wave crests accepted for computing celerity. The phase speed of each crest, computed by the best-fit slope (RANSAC) between two points in the 15m vicinity of each (x, t) coordinate along the curve, is interpolated onto a regular grid of 0.1m intervals. The same gridding discretization (0.1m, 0.1s) is used everywhere. At large offshore distances, a single video pixel can span multiple grid points, resulting in degraded accuracy. To address this issue, a pixel resolution cutoff is applied. Any pixel that covers more than 2 grid points is removed.

The ‘breakpoint transition’ (BP) method uses linear and nonlinear methods in their respective best areas by imposing a wave-by-wave step function γ_s as a function of cross-shore distance, with $\gamma_s = 0$ prior to breaking and $\gamma_s = 0.42$ post-breaking. The location of the breakpoint for each accepted wave track is determined heuristically (example given in Appendix B). The step function $\gamma_s = (0, 0.42)$ is imposed only at x -locations with at least 10% of the maximum number of phase speed estimates at any x -location during that hover (with the minimum number of estimates included typically between 5 and 11). The average of the individual $\gamma_s = (0, 0.42)$ step functions yields an effective $\gamma(x)$ (Fig. 3 e,f green line) that is used to define the “bad” (interpolated over) region for cBathy (Section 4.1). The transition from nonbreaking (here linear) to breaking, nonlinear domains through shoaling in the physical world is captured by the effective $\gamma(x)$ changing gradually from 0 to 0.42.

For each wave track, we invert for depth following linear shallow water theory $h = c^2/g$ (‘Linear’, Fig. 3), or with the nonlinear estimation (Eq. (3), with $\gamma = 0.42$ for ‘Nonlinear’, and γ_s for ‘BP’ in Fig. 3). The average depth is then computed from the individual tracks with a 5-m Gaussian smoothing applied. Following cBathy methodology, depths are then converted to an elevation (in NAVD88 datum) with a tidal offset, using the average water level over each UAV hover at the nearby La Jolla tide gauge (NOAA station 9410230).

4.4. Generating composite profiles

Profiles spanning from the shoreline to 10m depth (“composites”) are constructed by combining improved surf zone bathymetry estimates with cBathy offshore estimates (Fig. 4 d,h). The beginning of wave breaking (timestack derived, Appendix B) is used as the switching location between BP and cBathy estimates. Timestacks are used both to estimate surf zone depths and to define the shoreward limit of cBathy applicability, where cBathy and crest-tracking are joined. Example depth estimates have (Fig. 4 a-d) varying tidal level and approximately constant wave height and (Fig. 4 e-h) varying wave height and approximately the same tide level. The large surf zone depth errors ($\langle \text{RMSE} \rangle = 1.42\text{m}$, Fig. 4 a,e, Table 3) in raw, unfiltered cBathy are reduced by interpolating across the span identified as incorrect with timestacks (Fig. 4 b,f). Errors in the surf zone are further significantly reduced using the phase speeds of individual crests and applying a depth inversion individually before smoothing (Gaussian-weighted 5-m moving average) and averaging (Fig. 4 c,g).

A subaerial beach profile obtained from a low tide RTK-GNSS survey is combined with the subaqueous bathymetry to obtain a full profile (Fig. 4 d,h). When both the survey and bathymetric estimations are available in the same cross-shore location, the low-tide survey is preferentially selected. By overriding the inner surf zone/swash zone bathymetry results with a ground-truth survey, we avoid potential issues with wave setup or large depth over-estimations near the shoreline (Sénéchal et al., 2004; Power et al., 2010; Fiedler et al., 2021). If no overlapping region between survey and bathymetry estimates exists, the distance between the two are linearly interpolated. The composite profile has smaller errors ($\langle \text{RMSE} \rangle$ and $\langle \text{Bias} \rangle$) in $< 3\text{m}$ depth than either cBathy version. Composite profile normalized errors ($\langle \text{RMSE} \rangle/h$) vary between 0.1 – 0.2, with largest values near the shoreline (Fig. 5).

Table 3

RMSE and Bias statistics for composite models (depth $< 10\text{m}$) at Torrey Pines. surf zone goes from the beginning of wave breaking to the SWL line. Offshore goes from the beginning of wave breaking to 500 m offshore.

Composites	cBathy (hErr < 0.5 m)	cBathy (breaking parameter)	cBathy (nonlinear)	cBathyCT
$\langle \text{RMSE} \rangle$ (m)				
Surf zone	0.81	0.55	0.44	0.17
Offshore	0.90	0.90	0.92	0.87
Full profile	0.9	0.79	0.76	0.68
$\langle \text{Bias} \rangle$ (m)				
Surf zone	−0.56	−0.41	−0.29	0.06
Offshore	0.58	0.58	0.61	0.58
Full profile	0.12	0.19	0.25	0.38

RMSE values offshore of the surf zone are similar because all methods use cBathy. The mean RMSE varied between 0.05 – 1.75m depending on conditions (including UAV height, lighting, Hs and other factors). Although using $\gamma(x)$ to determine the bounds of the surf zone for interpolation within cBathy (rather than hErr) improves the estimates, only breakpoint crest-tracking accurately captures the terrace in a single hover.

5. Discussion

5.1. Error sources

(Holman et al., 2013) proposed mitigating the surf zone gap in cBathy by Kalman filtering cBathy estimations together, based on hErr, over a tidal cycle. However, tidal variation from -0.27 – 1.13 NAVD88 m did not shift the surf zone gap location sufficiently to span the full profile (Fig. 4 a). Rather than simply a shoreward shift of a constant width surf zone as on a plane beach, the observed surf zone both widened and shifted onshore. The location where cBathy estimates fail changes with tidal elevation (Fig. 6) but not enough to generate a full accurate bathymetry from cBathy alone. Kalman results computed with 07/07/2020 data over a tidal cycle only improved results slightly. Composite profiles are relatively insensitive to tide level (Fig. 4 d).

The largest (un-normalized) $\langle \text{RMSE} \rangle$ and $\langle \text{Bias} \rangle$ are in the deepest water $h = 8 - 10\text{m}$ (Fig. 5, Table 3) where historical ground-truth (not shown) depths change relatively little ($\langle \text{RMSE} \rangle \sim 0.5\text{m}$). Offshore errors could be reduced using historical insitu profiles to constrain the range of plausible offshore depths. The extent to which previous ground truth profiles improve remote estimates (e.g. Kalman filtering) depends on both the characteristics of the available insitu bathymetry and the beach variability. Kalman filtering is most effective for a beach that is known (from past, extensive, accurate surveys) to change little, or to change predictably in response to changing wave conditions.

UAV rectification uses ground (stability) control points that are limited to the bottom of the field of view, approximately in a straight line, and rarely near the image offshore edge. The resulting roll and pitch errors are corrected with a cross-shore shift (mean shift = 5.4m) when combining remotely-sensed subaqueous and observed subaerial surveys. Including horizon tracking to the least-squares fitting of the camera extrinsics might reduce these offsets and errors in the deepest water (Bergsma et al., 2019; Tsukada et al., 2020).

Normal incidence is not assumed in cBathy, but is assumed with surf zone crest-tracking using timestacks. Waves in the present dataset are primarily normally incident with the largest 10m-depth wave obliquity at Torrey Pines at 12° (Table 1). Assuming Snell’s Law, and using 5m as a maximum surf zone depth, errors from neglecting wave obliquity are usually less than 2%. Larger wave obliquities may lead to more obvious overestimation of phase speeds and depth, however, the current dataset limits testing the crest-tracking (CT) part of cBathyCT for obliquely incident waves. Similarly, seas with very broad spectra and

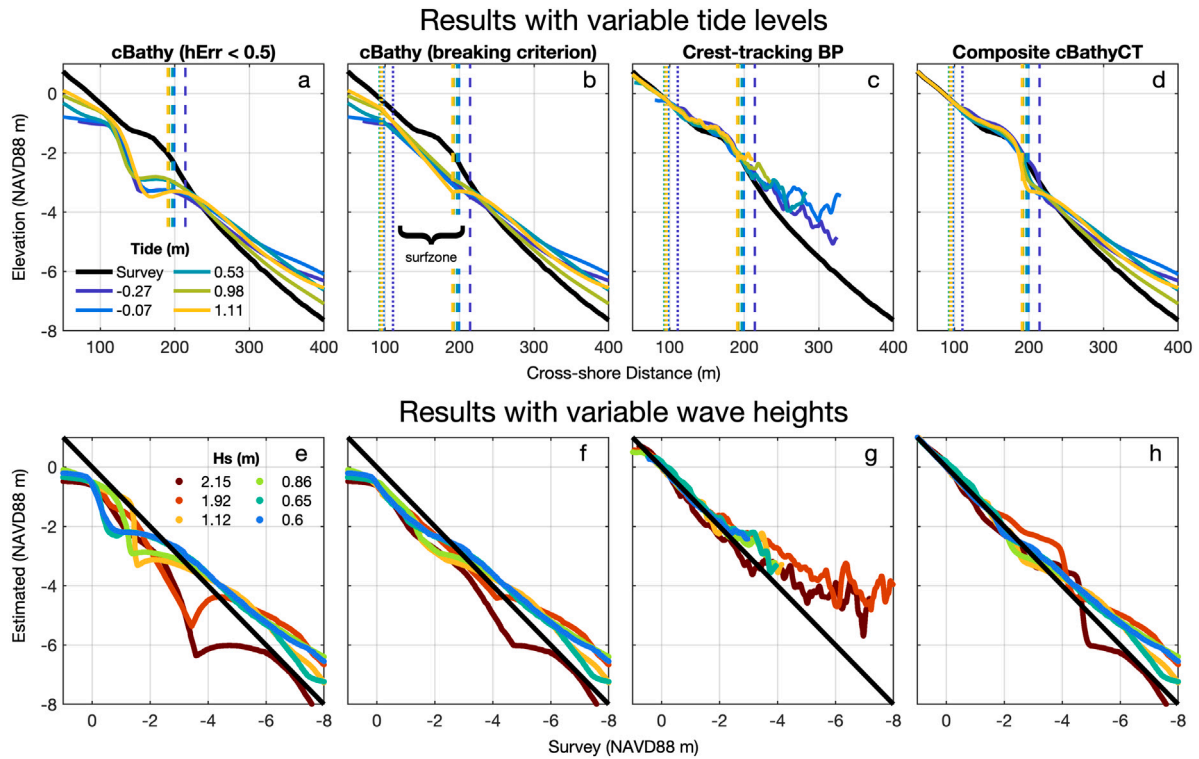


Fig. 4. Bathymetry estimates at Torrey Pines MOP 582. Upper panels show July 7th, 2020 elevation versus cross-shore distance for varying tide levels (1.3m max difference, legend). The dotted vertical line (upper panels) marks the shoreward edge of surf zone and offshore extent of subaerial survey where the crest tracking method (c,g) is fused with insitu data for composite cBathyCT (d,h). Vertical dashed lines mark beginning of wave breaking where cBathy (b,f) and crest-tracking bathymetry (c,g) are stitched together to form the composite (d,h). Bottom panels show estimated versus observed elevation for varying wave heights (legend) near mid-tide on various dates (Table 1). Solid black is ground truth. Bathymetry estimates are shown from cBathy interpolated over $hErr < 0.5$ (a,e), cBathy interpolated over the breaking region (b,f), breakpoint transition crest-tracking (c,g) and cBathyCT (d,h). Owing to the non-planar beach profile, the stitching location varied little with tide (top panel, dotted line). Fit statistics for various composites are in Table 3.

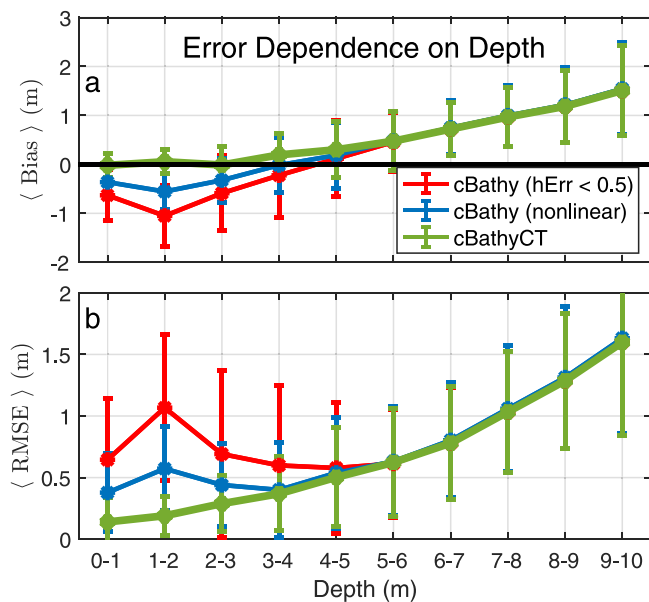


Fig. 5. Torrey Pines composite bathymetry mean statistics from 59 full profiles, binned by depth (solid curves). (top) mean Bias, (bottom) mean RMSE. Curve color indicates surf zone method: (red) cBathy estimate with $hErr < 0.5$ m, (blue) cBathy with breaking criterion for surf zone interpolation and nonlinear gamma correction, (green) cBathy with breakpoint transition crest-tracking in the surf zone (cBathyCT). Seaward of breaking, methods all use cBathy and curves overlap. Depth is relative to the still water line, accounting for tides but not setup. Error bars show standard deviation. For cBathyCT composite, the normalized standard $\langle RMSE \rangle / h = 0.27, 0.13, 0.11$, and 0.15 for bin centered on $0.5, 1.5, 4.5$, and 8.5 m respectively.

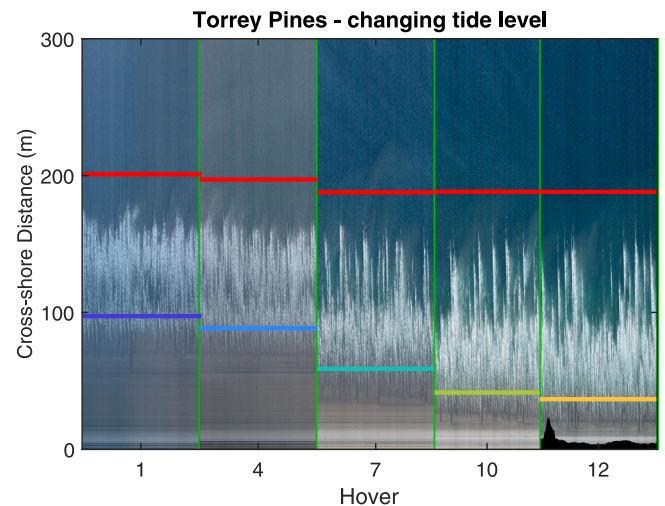


Fig. 6. Torrey Pines MOP 582 on July 7th, 2020. Wave height $H_s \sim 0.89$ m. Timestacks (intensity versus time on a cross-shore transect) for 5, 17-minute hovers during flood tide, separated by green vertical lines. The waterline (colored horizontal lines, Fig. 5 a) gradually moves onshore 60m (from $x = 97$ m to 37 m) during flood (1.37 m tide increase). The shoreward limit of accurate cBathy (solid red lines) includes breaking in the 50m-wide sample window. The offshore boundary moves onshore only 12m (from $x = 200$ m to 188 m) owing to a small terrace (Fig. 2) that triggers breaking.

therefore many different celerities present in a single timestack may lead to bad estimates with the present surf zone correction. cBathy Phase 1 frequency–wavenumber pairs can be used to determine the appropriateness of a narrow spectrum assumption, by identifying the

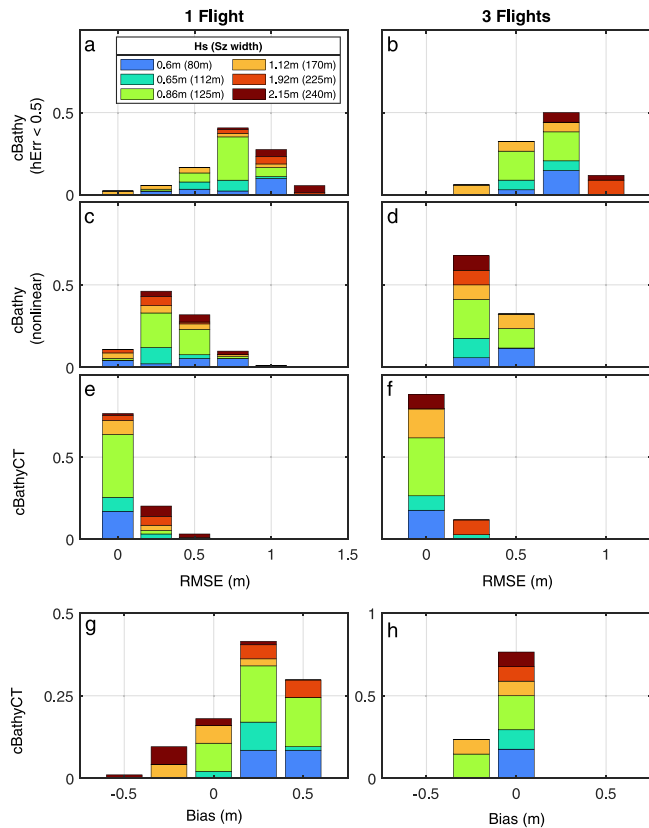


Fig. 7. Histograms of depth inversion errors at Torrey Pines (for the surf zone region) for different methods (stacked vertically) on 59 transects (left) 1 hover and (right) median of 3 hovers. (a,b) cBathy with interpolation where $hErr < 0.5m$, (c,d) cBathy with breaking criterion for surf zone interpolation and nonlinear gamma correction, and (e,f) composite using breakpoint crest-tracking cBathyCT, (g,h) mean bias of cBathyCT. Colored by offshore H_s (legend). Outliers with the largest bias and RMSE are removed with 3 hovers. Fit statistics in Table 3. Probabilities (vertical axis) sum to 1.0.

frequency spread of the 4 most coherent frequencies. Further testing of the method in a larger variety of wave conditions is required to determine the limits of both the normal incidence and narrow spectrum assumptions.

The shallow water approximation for c used in crest-tracking is valid in the present depths ($< 5m$) with long-period swell ($T_p > 9sec$) but finite depth theory could readily be used. The peak period as determined from the timestack and a nearby buoy in 17m depth (NOAA NDBC Station 46266) usually differs by less than 1s. Outliers in single hovers are removed by using the median of 3 flights rather than a single flight (Fig. 7), but overall statistics do not consistently improve. Full profile single-hover profile bias is low owing to cancelling errors ($\langle RMSE \rangle$ is high) (Table 3).

5.2. Applicability to other sites

Pre-training a U-Net network on a large surf zone dataset provides the network with a good general feature representation. Additional training would be needed for sites with much different incident waves or breaking wave characteristics. A strength of the present methodology is that deep learning is only used as an annotation tool, automating the extraction of crest speeds from timestack-image wave detection, while allowing for depth estimates from different wave dispersion models (here Eq. (1)–(3)).

The crest-tracking BP method performs similarly (to Torrey Pines) on the terraced profile at SIO (Fig. 2), with mean $\langle RMSE \rangle = 0.08m$ and $\langle Bias \rangle = -0.02m$ in the surf zone. Performance was also good at

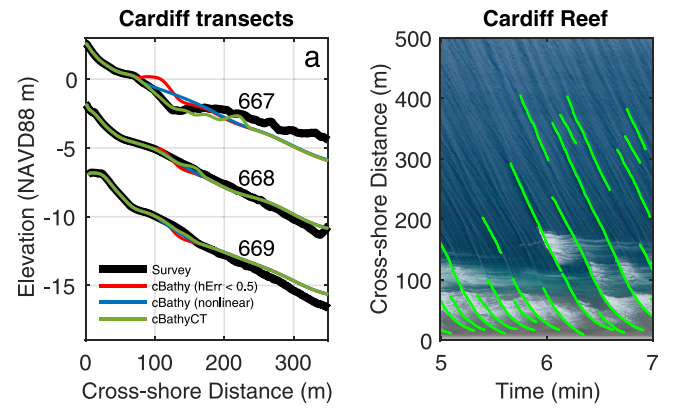


Fig. 8. (left) Depth versus cross-shore distance from 1 hover on MOP 667 - 669 (stacked with a 5 m vertical offset). Ground truth (black), cBathy with $hErr < 0.5m$ (red), cBathy with a nonlinear correction (blue) and cBathyCT (green). Bedrock reef on MOP 667 from $x = 125m$ to $\sim 1km$ offshore. (right) Results of the deep-learning crest-tracking algorithm on MOP 667. The wave crest detection neural network was not trained on reef-like profiles, but may detect wave crests accurately enough for use in alternative (e.g. 2D nonlinear) depth inversions.

Cardiff on MOP 668, 669, but was degraded by a bedrock reef at the southern edge of the field of view (MOP 667, Fig. 8 a). The wave detection algorithm annotates the images accurately (Fig. 8 b), but the estimation and inversion from c to depth is inadequate. Nonlinear frequency doubling (e.g. Elgar et al., 1997) on the flat terrace (between $x = 120m$ and $200m$, Fig. 8 a) may create additional crests that would confound simple crest-conserving inversions.

The effect of alongshore variations in bathymetry on phase speed and crest direction is neglected here, but could be included in more sophisticated 2D inversions both within and seaward of the surf zone.

The $\gamma = 0.42$ used here is based on historical observations at Torrey Pines (Thornton and Guza, 1982). LiDAR wavescans concurrent with UAV hovers yield a local $\gamma(x)$ (Fig. 9 b-d), computed from direct sea surface elevation measurements (H_{m0}) and insitu surveys (Fiedler et al., 2021). The average γ over the surf zone varies between $0.55 - 0.74$, decreasing offshore. Deviations in gamma estimations at these sites do not significantly affect the bathymetric estimations; mean $\langle RMSE \rangle = 0.25m$ is minimum over all available transects for $0.4 < \gamma < 0.5$, increasing only slightly to $0.3m$ for $0.6 < \gamma < 0.8$. The median bias is minimum for γ between 0.3 and 0.5 (Fig. 9 a). Yoo et al. (2011) reported $\gamma = 0.6$ in their crest-tracking study. Note in 'low' wave conditions ($H_s < 0.75m$), linear crest-tracking ($\gamma = 0$) and BP perform comparably well with $\langle RMSE \rangle \sim 0.18m$ in the breaking region. Not surprisingly, corrections for wave nonlinearity are most important when H_s is largest.

6. Conclusions

This paper presents an improved method for estimating nearshore bathymetry (from the subaerial beach to $\sim 10m$ depth) from a single relatively short (17-minute) drone video in four steps. A cross-shore depth profile is obtained from a hovering video by (1) using cBathy (Holman et al., 2013; Holman and Bergsma, 2021) for the region offshore of the surf zone, (2) using a neural network to obtain wave crest annotations from timestack images, (3) estimating the surfzone depth from timestack wave celerity and a simple nonlinear correction, and (4) combining these results and the subaerial beach (e.g. from Structure-from-Motion), based on the location of wave breaking. Each of these individual steps can be modified when new developments occur. In its current form, cBathyCT results have $\langle RMSE \rangle = 0.68m$ and $\langle Bias \rangle = 0.38m$ across the full profile, from subaerial beach to $10m$ depth. Within the surfzone $\langle RMSE \rangle$ reduces from $0.81m$ with cBathy v2.0 to $0.17m$ with cBathyCT.

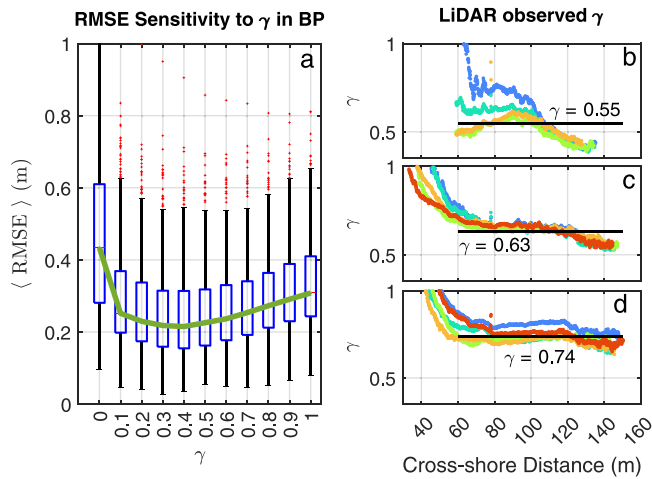


Fig. 9. (left) for 468 transects, median RMSE versus γ (green curve), (boxes) 50% quantile, (black bars) 90% quantile for crest-tracking BP method in the surf zone (outliers red dots). Minimum $\langle \text{RMSE} \rangle$ at $\gamma = 0.4$ increases $< 20\%$ for $0.1 < \gamma < 0.7$. (right) surf zone LiDAR measured $\gamma = H_{m0}/h$ versus cross-shore distance for (b) Nov 2nd, 2021, $H_s = 1.12\text{m}$, (c) Oct 26th, 2021, $H_s = 1.92\text{m}$, (d) Dec 15th, 2021, $H_s = 2.15\text{m}$, colored by hover. Black horizontal line is mean γ over surf zone.

Results for individual 17-minute hovers are encouraging. The dependence of cBathy and crest-tracking error statistics (e.g. $\langle \text{RMSE} \rangle$) on record length is unknown, and likely varies with wave conditions and bathymetry. Errors in composite profiles do not depend significantly on tide level for the present limited range of conditions but may depend on tide level on barred bathymetry. In addition, the present approach ($\gamma = 0.42$) likely fails in shallow water on steep slopes where plunging waves with $\gamma > 0.8$ are expected. Concurrent video and LiDAR (e.g. Fig. 9) of γ and c would enable application of the present method to sites with much different breaking wave characteristics and γ . Additional model testing and calibration is needed and ongoing.

cBathyCT is a (by-design) simple method for addressing the known issues with the existing cBathy algorithm and providing automated nearshore bathymetry profiles from single UAV flights. Here we have shown that the resulting composite profiles usefully improve bathymetry estimations for our test sites. By resolving this critical gap in surf-zone bathymetry estimation, cBathyCT serves as an incremental advancement in hazard assessment at southern California beaches.

CRediT authorship contribution statement

Athina M.Z. Lange: Conceptualization, Investigation, Formal analysis, Writing – original draft, Visualization. **Julia W. Fiedler:** Conceptualization, Methodology, Writing – review & editing. **Mark A. Merrifield:** Conceptualization, Writing – review & editing, Funding acquisition. **R.T. Guza:** Conceptualization, Writing – review & editing.

Declaration of competing interest

The authors declare that they have no known competing financial interests or personal relationships that could have appeared to influence the work reported in this paper.

Data availability

I have shared the GitHub repository with the code and sample data in the manuscript.

Acknowledgments

This study was funded by the U.S. Army Corps of Engineers (W912 HZ1920020) and the California Department of Parks and Recreation (C19E0026). Data were collected and processed by the Coastal Processes Group field team members Lucian Parry, Rob Grenzeback, Kent Smith, Brian Woodward, Greg Boyd, and Mele Johnson. Michele Okihiro organized logistics.

Appendix A. Wave-crest detection deep learning algorithm

The U-Net architecture (Ronneberger et al., 2015) is well established for segmentation tasks such as crest detection. U-Nets are based on an Encoder-Decoder architecture, with skip connections from the Encoder to the Decoder at the different levels to be able to recover resolution. The Encoder provides a compact feature representation (many features, but little resolution) of the input image by applying convolutions followed by a maxpool downsampling at multiple levels (more features, less resolution). The Decoder takes the compact feature representation and provides a classification for each pixel in the image at full resolution by upsampling followed by concatenation and convolutions at multiple levels (fewer features, more resolution). We used a modified version of the U-Net with a ResNet18 encoder pre-trained on the ImageNet dataset (Usuyama, 2018) (Fig. 10).

Wave crest detection uses a limited neighborhood area in timestack-images. Training and prediction can use small high-resolution image tiles, increasing the training dataset size and reducing the deep learning network complexity. To augment the training dataset, image tiles are sampled at arbitrary locations in the image. Timestack-images are 5000 pixels cross-shore direction and a time-dependent width of 600 pixels per minute. For the training, we sample 1000 256×256 image tiles from a timestack-image. For the prediction, we divide the timestack-image into overlapping 256×256 image tiles. The border of the predicted image tiles (therefore the overlap) has relatively large errors and is not used. Thresholds such as minimum length and width of detected track can be specified.

A binary cross-entropy (BCE) loss function is used for binary classification (limited to a region around the sparse ground-truth), with a Root-Mean-Square (RMS) optimizer and an adaptive learning rate scheduler. The model is trained for 50 epochs, with a batch size of 8 and an initial adaptive learning rate of 0.0001. Training and validation losses remained constant after 40 epochs. Model predictions are made after 50 epochs. The deep learning approach was implemented in Python and PyTorch. A desktop computer with a GeForce GTX 1660 GPU required 50 hours to train the model for 50 epochs, with predictions taking 2.5 minutes per timestack.

Appendix B. Breakpoint locator

The breakpoint location is determined with an algorithm based on pixel intensity gradients along a wave track. Thresholds for broken and unbroken waves are determined by fitting two Gaussian distributions to the image pixel intensity histograms (Fig. 11 a) and determining the mean of the distributions. Individual waves track may include only broken or only unbroken waves, with relatively small gradients, and high or low pixel intensity levels (red and black circles respectively, Fig. 11 a). Tracks that include the breakpoint begin unbroken (below the low threshold), with a sharp gradient (purple dot, Fig. 11 c) when breaking begins, and a high but stable pixel intensity above the high threshold (green circle, Fig. 11 b). The breakpoint location is set to the location of maximum gradient. Residual foam can obscure sharp breakpoint gradients, and each wave track goes through an iterative process to determine if it contains the breakpoint. Failing a conclusive result with the first pass with the strictest thresholds, less stringent thresholds are applied until the segment is characterized (examples provided in the attached code). The breaking location estimated by the algorithm and visual inspection agree.

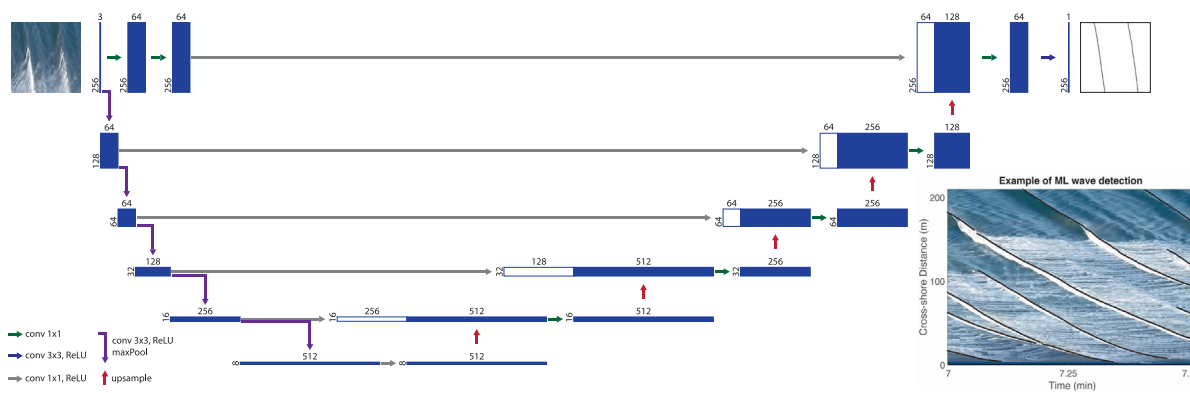


Fig. 10. Wave Crest Detection U-Net Architecture: Blue boxes correspond to the feature map, and white, the copied feature map from the Encoder. The number of features is given on top of the box and resolution (number of pixels) to the left. Gray arrows indicate skip connections. Arrows indicate the corresponding convolution. (inserts) Example of ML wave crest detection.

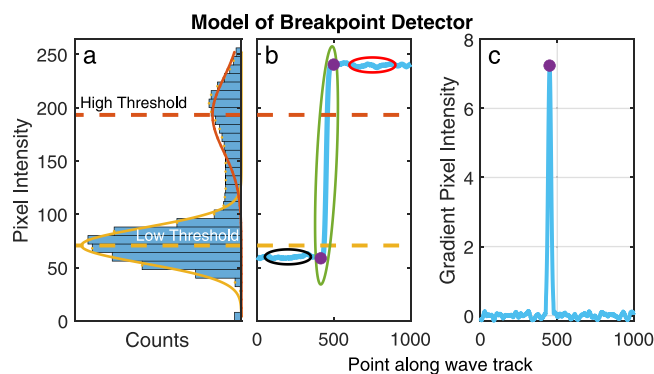


Fig. 11. Schematic of breakpoint location using gradients of pixel intensity. (left) histogram of pixel intensity of the full image (10^7 counts are shown) typically have two maxima and each is fit to a Gaussian distribution, centered around high and low thresholds (red and yellow respectively). (middle) idealized pixel intensity versus location on wave track segment completely within (all broken) or completely seaward (unbroken) of surf zone (red and black circles, respectively). Sharp gradients (green) indicate breakpoint. (right) idealized pixel intensity gradient versus along-track location.

References

- Aarninkhof, S.G.J., 2005. Nearshore subtidal bathymetry from time-exposure video images. *J. Geophys. Res.* 110 (C6), C06011. <http://dx.doi.org/10.1029/2004JC002791>, URL: <http://doi.wiley.com/10.1029/2004JC002791>.
- Abileah, R., Trizna, D.B., 2010. Shallow water bathymetry with an incoherent X-band radar using small (smaller) space-time image cubes. In: 2010 IEEE International Geoscience and Remote Sensing Symposium. IEEE, Honolulu, HI, USA, pp. 4330–4333. <http://dx.doi.org/10.1109/IGARSS.2010.5654386>, URL: <http://ieeexplore.ieee.org/document/5654386/>.
- Almar, R., Bonneton, P., Senechal, N., Roelvink, D., 2009. WAVE CELERITY FROM VIDEO IMAGING: A NEW METHOD. In: Coastal Engineering 2008. World Scientific Publishing Company, Hamburg, Germany, pp. 661–673. http://dx.doi.org/10.1142/9789814277426_0056, URL: http://www.worldscientific.com/doi/abs/10.1142/9789814277426_0056.
- Basco, D.R., 1985. A Qualitative Description of Wave Breaking. *J. Waterw. Port Coast. Ocean Eng.* 111 (2), 171–188.
- Bergsma, E.W., Almar, R., Melo de Almeida, L.P., Sall, M., 2019. On the operational use of UAVs for video-derived bathymetry. *Coast. Eng.* 152, 103527. <http://dx.doi.org/10.1016/j.coastaleng.2019.103527>, URL: <https://linkinghub.elsevier.com/retrieve/pii/S0378383918303582>.
- Bergsma, E., Conley, D., Davidson, M., O'Hare, T., 2016. Video-based nearshore bathymetry estimation in macro-tidal environments. *Mar. Geol.* 374, 31–41. <http://dx.doi.org/10.1016/j.margeo.2016.02.001>, URL: <https://linkinghub.elsevier.com/retrieve/pii/S0025322716300159>.
- Brodie, K.L., Bruder, B.L., Slocum, R.K., Spore, N.J., 2019. Simultaneous Mapping of Coastal Topography and Bathymetry From a Lightweight Multicamera UAS. *IEEE Trans. Geosci. Remote Sens.* 57 (9), 6844–6864. <http://dx.doi.org/10.1109/TGRS.2019.2909026>, URL: <https://ieeexplore.ieee.org/document/8726410/>.
- Brodie, K.L., Palmsten, M.L., Hesser, T.J., Dickhudt, P.J., Raubenheimer, B., Ladner, H., Elgar, S., 2018. Evaluation of video-based linear depth inversion performance and applications using altimeters and hydrographic surveys in a wide range of environmental conditions. *Coast. Eng.* 136, 147–160. <http://dx.doi.org/10.1016/j.coastaleng.2018.01.003>, URL: <https://linkinghub.elsevier.com/retrieve/pii/S0378383917301989>.
- Bruder, B.L., Brodie, K.L., 2020. CIRC Quantitative Coastal Imaging Toolbox. SoftwareX 12, 100582. <http://dx.doi.org/10.1016/j.softx.2020.100582>, URL: <https://linkinghub.elsevier.com/retrieve/pii/S2352711020302958>.
- Catalán, P.A., Haller, M.C., 2008. Remote sensing of breaking wave phase speeds with application to non-linear depth inversions. *Coast. Eng.* 55 (1), 93–111. <http://dx.doi.org/10.1016/j.coastaleng.2007.09.010>, URL: <https://linkinghub.elsevier.com/retrieve/pii/S0378383907001007>.
- Collins, A., Brodie, K., Bak, A.S., Hesser, T., Farthing, M., Lee, J., Long, J., 2020. Bathymetric Inversion and Uncertainty Estimation from Synthetic Surf-Zone Imagery with Machine Learning. *Remote Sens.* 12 (20), 3364. <http://dx.doi.org/10.3390/rs12203364>, URL: <https://www.mdpi.com/2072-4292/12/20/3364>.
- van Dongeren, A., Plant, N., Cohen, A., Roelvink, D., Haller, M.C., Catalán, P., 2008. Beach Wizard: Nearshore bathymetry estimation through assimilation of model computations and remote observations. *Coast. Eng.* 55 (12), 1016–1027. <http://dx.doi.org/10.1016/j.coastaleng.2008.04.011>, URL: <https://linkinghub.elsevier.com/retrieve/pii/S0378383908000884>.
- Elgar, S., Guza, R.T., Raubenheimer, B., Herbers, T.H.C., Gallagher, E.L., 1997. Spectral evolution of shoaling and breaking waves on a barred beach. *J. Geophys. Res.: Oceans* 102 (C7), 15797–15805. <http://dx.doi.org/10.1029/97JC01010>, URL: <http://doi.wiley.com/10.1029/97JC01010>.
- Fiedler, J.W., Kim, L., Grenzbeck, R., Young, A., Merrifield, M.A., 2021. Enhanced Surf Zone and Wave Runup Observations with Hovering Drone-Mounted Lidar. *J. Atmos. Ocean. Technol.* 38 (11), 1967–1978. <http://dx.doi.org/10.1175/JTECH-D-21-0027.1>, URL: <https://journals.ametsoc.org/view/journals/atot/38/11/JTECH-D-21-0027.1.xml>.
- Gao, J., 2009. Bathymetric mapping by means of remote sensing: methods, accuracy and limitations. *Prog. Phys. Geogr. Earth Environ.* 33 (1), 103–116. <http://dx.doi.org/10.1177/0309133309105657>, URL: <http://journals.sagepub.com/doi/10.1177/0309133309105657>.
- Geyman, E.C., Maloof, A.C., 2019. A Simple Method for Extracting Water Depth From Multispectral Satellite Imagery in Regions of Variable Bottom Type. *Earth Space Sci.* 6 (3), 527–537. <http://dx.doi.org/10.1029/2018EA000539>, URL: <https://onlinelibrary.wiley.com/doi/abs/10.1029/2018EA000539>.
- Gomes da Silva, P., Coco, G., Garnier, R., Klein, A.H., 2020. On the prediction of runup, setup and swash on beaches. *Earth-Sci. Rev.* 204, 103148. <http://dx.doi.org/10.1016/j.earscirev.2020.103148>, URL: <https://linkinghub.elsevier.com/retrieve/pii/S0012825219306828>.
- Holland, T., 2001. Application of the linear dispersion relation with respect to depth inversion and remotely sensed imagery. *IEEE Trans. Geosci. Remote Sens.* 39 (9), 2060–2072. <http://dx.doi.org/10.1109/36.951097>, URL: <http://ieeexplore.ieee.org/document/951097/>.
- Holman, R., Bergsma, E.W.J., 2021. Updates to and Performance of the cBathy Algorithm for Estimating Nearshore Bathymetry from Remote Sensing Imagery. *Remote Sens.* 13 (19), 3996. <http://dx.doi.org/10.3390/rs13193996>, URL: <https://www.mdpi.com/2072-4292/13/19/3996>.
- Holman, R., Haller, M.C., 2013. Remote Sensing of the Nearshore. *Ann. Rev. Mar. Sci.* 5 (1), 95–113. <http://dx.doi.org/10.1146/annurev-marine-121211-172408>, URL: <http://www.annualreviews.org/doi/10.1146/annurev-marine-121211-172408>.
- Holman, R., Plant, N., Holland, T., 2013. cBathy: A robust algorithm for estimating nearshore bathymetry: The cBathy Algorithm. *J. Geophys. Res.: Oceans* 118 (5), 2595–2609. <http://dx.doi.org/10.1002/jgrc.20199>, URL: <http://doi.wiley.com/10.1002/jgrc.20199>.

- Holman, R., Stanley, J., 2007. The history and technical capabilities of Argus. *Coast. Eng.* 54 (6–7), 477–491. <http://dx.doi.org/10.1016/j.coastaleng.2007.01.003>, URL: <https://linkinghub.elsevier.com/retrieve/pii/S037838390700018X>.
- Inman, D.L., Tait, R.J., Nordstrom, C.E., 1971. Mixing in the surf zone. *J. Geophys. Res.* 76 (15), 3493–3514. <http://dx.doi.org/10.1029/JC076i015p03493>, URL: <http://doi.wiley.com/10.1029/JC076i015p03493>.
- Jing, E., Datt, B., 2010. Detection of coastal bathymetry using hyperspectral imagery. In: *OCEANS'10 IEEE SYDNEY*. IEEE, Sydney, Australia, pp. 1–4. <http://dx.doi.org/10.1109/OCEANSSYD.2010.5603864>, URL: <http://ieeexplore.ieee.org/document/5603864/>.
- Jordi, A., Georgas, N., Blumberg, A., Yin, L., Chen, Z., Wang, Y., Schulte, J., Ramaswamy, V., Runnels, D., Saleh, F., 2019. A Next-Generation Coastal Ocean Operational System: Probabilistic Flood Forecasting at Street Scale. *Bull. Am. Meteorol. Soc.* 100 (1), 41–54. <http://dx.doi.org/10.1175/BAMS-D-17-0309.1>, URL: <https://journals.ametsoc.org/view/journals/bams/100/1/bams-d-17-0309.1.xml>.
- Legleiter, C.J., Harrison, L.R., 2019. Remote Sensing of River Bathymetry: Evaluating a Range of Sensors, Platforms, and Algorithms on the Upper Sacramento River, California, USA. *Water Resour. Res.* 55 (3), 2142–2169. <http://dx.doi.org/10.1029/2018WR023586>, URL: <https://onlinelibrary.wiley.com/doi/abs/10.1029/2018WR023586>.
- Li, J., Knapp, D.E., Schill, S.R., Roelfsema, C., Phinn, S., Silman, M., Mascaro, J., Asner, G.P., 2019. Adaptive bathymetry estimation for shallow coastal waters using Planet Dove satellites. *Remote Sens. Environ.* 232, 111302. <http://dx.doi.org/10.1016/j.rse.2019.111302>, URL: <https://linkinghub.elsevier.com/retrieve/pii/S0034425719303219>.
- Lippmann, T.C., Holman, R.A., 1989. Quantification of sand bar morphology: A video technique based on wave dissipation. *J. Geophys. Res.* 94, 17.
- Lippmann, T.C., Holman, R., 1991. Phase Speed and Angle of Breaking Waves Measured with Video Techniques, Vol. 1. pp. 542–556.
- Mallet, C., Bretar, F., 2009. Full-waveform topographic lidar: State-of-the-art. *ISPRS J. Photogramm. Remote Sens.* 64 (1), 1–16. <http://dx.doi.org/10.1016/j.isprsjprs.2008.09.007>, URL: <https://linkinghub.elsevier.com/retrieve/pii/S0924271608000993>.
- Martins, K., Blenkinsopp, C.E., Deigaard, R., Power, H.E., 2018. Energy Dissipation in the Inner Surf Zone: New Insights From LiDAR -Based Roller Geometry Measurements. *J. Geophys. Res.: Oceans* 123 (5), 3386–3407. <http://dx.doi.org/10.1029/2017JC013369>, URL: <https://onlinelibrary.wiley.com/doi/abs/10.1029/2017JC013369>.
- Merrifield, M.A., Johnson, M., Guza, R.T., Fiedler, J.W., Young, A.P., Henderson, C., Lange, A.M., O'Reilly, W.C., Ludka, B.C., Okihito, M., Pappas, K., Engeman, L., Behrens, J., Terrill, E., 2021. An early warning system for wave-driven coastal flooding at Imperial Beach, CA. *Nat. Hazards*.
- O'Reilly, W., Olfe, C.B., Thomas, J., Seymour, R., Guza, R., 2016. The California coastal wave monitoring and prediction system. *Coast. Eng.* 116, 118–132. <http://dx.doi.org/10.1016/j.coastaleng.2016.06.005>, URL: <https://linkinghub.elsevier.com/retrieve/pii/S0378383916301120>.
- Plant, N.G., Edwards, K.L., Kaihatu, J.M., Veeramony, J., Hsu, L., Holland, K.T., 2009. The effect of bathymetric filtering on nearshore process model results. *Coast. Eng.* 56 (4), 484–493. <http://dx.doi.org/10.1016/j.coastaleng.2008.10.010>, URL: <https://linkinghub.elsevier.com/retrieve/pii/S0378383908001841>.
- Power, H.E., Hughes, M.G., Aagaard, T., Baldock, T.E., 2010. Nearshore wave height variation in unsaturated surf. *J. Geophys. Res.* 115 (C8), C08030. <http://dx.doi.org/10.1029/2009JC005758>, URL: <http://doi.wiley.com/10.1029/2009JC005758>.
- Radermacher, M., Wengrove, M., van Thiel de Vries, J., Holman, R., 2014. Applicability of video-derived bathymetry estimates to nearshore current model predictions. *J. Coast. Res.* 70, 290–295. <http://dx.doi.org/10.2112/SI70-049.1>, URL: <http://www.bioone.org/doi/10.2112/SI70-049.1>.
- Raubenheimer, B., Guza, R.T., Elgar, S., 1996. Wave transformation across the inner surf zone. *J. Geophys. Res.: Oceans* 101 (C11), 25589–25597. <http://dx.doi.org/10.1029/96JC02433>, URL: <http://doi.wiley.com/10.1029/96JC02433>.
- Ronneberger, O., Fischer, P., Brox, T., 2015. U-Net: Convolutional Networks for Biomedical Image Segmentation. <http://arxiv.org/abs/1505.04597> [cs].
- Rutten, J., de Jong, S.M., Ruessink, G., 2017. Accuracy of Nearshore Bathymetry Inverted From \$(X)\$-Band Radar and Optical Video Data. *IEEE Trans. Geosci. Remote Sens.* 55 (2), 1106–1116. <http://dx.doi.org/10.1109/TGRS.2016.2619481>, URL: <http://ieeexplore.ieee.org/document/7738400/>.
- Sénéchal, N., Dupuis, H., Bonneton, P., 2004. Preliminary hydrodynamic results of a field experiment on a barred beach, True Vert beach on October 2001. *Ocean Dyn.* 54, 408–414. <http://dx.doi.org/10.1007/s10236-003-0052-9>.
- Stephens, E., Cloke, H., 2014. Improving flood forecasts for better flood preparedness in the UK (and beyond): Commentary. *Geogr. J.* 180 (4), 310–316. <http://dx.doi.org/10.1111/geoj.12103>, URL: <http://doi.wiley.com/10.1111/geoj.12103>.
- Stive, M.J.F., 1980. VELOCITY AND PRESSURE FIELD OF SPILLING BREAKERS. *Coast. Eng.* 20.
- Stockdon, H.F., Holman, R.A., 2000. Estimation of wave phase speed and nearshore bathymetry from video imagery. *J. Geophys. Res.: Oceans* 105 (C9), 22015–22033. <http://dx.doi.org/10.1029/1999JC000124>, URL: <http://doi.wiley.com/10.1029/1999JC000124>.
- Stokes, K., Poate, T., Masselink, G., 2019. DEVELOPMENT OF a REAL-TIME, REGIONAL COASTAL FLOOD WARNING SYSTEM FOR SOUTHWEST England. In: *Coastal Sediments 2019*. World Scientific, Tampa/St. Petersburg, Florida, USA, pp. 1460–1474. http://dx.doi.org/10.1142/9789811204487_0127, URL: https://www.worldscientific.com/doi/abs/10.1142/9789811204487_0127.
- Stokes, K., Poate, T., Masselink, G., King, E., Saulter, A., Ely, N., 2021. Forecasting coastal overtopping at engineered and naturally defended coastlines. *Coast. Eng.* 164, 103827. <http://dx.doi.org/10.1016/j.coastaleng.2020.103827>, URL: <https://linkinghub.elsevier.com/retrieve/pii/S0378383920305135>.
- Stringari, C., Harris, D., Power, H., 2019. A novel machine learning algorithm for tracking remotely sensed waves in the surf zone. *Coast. Eng.* 147, 149–158. <http://dx.doi.org/10.1016/j.coastaleng.2019.02.002>, URL: <https://linkinghub.elsevier.com/retrieve/pii/S037838391830228X>.
- Svendsen, I.A., Buhr Hansen, J., 1976. Deformation up to Breaking of Periodic Waves on a Beach. In: *Proceedings, 15th International Conference on Coastal Engineering*. pp. 520–539.
- Svendsen, I.A., Qin, W., Ebersole, B.A., 2003. Modelling waves and currents at the LSTF and other laboratory facilities. *Coast. Eng.* 50 (1–2), 19–45. [http://dx.doi.org/10.1016/S0378-3839\(03\)00077-2](http://dx.doi.org/10.1016/S0378-3839(03)00077-2), URL: <https://linkinghub.elsevier.com/retrieve/pii/S0378383903000772>.
- Szeliski, R., 2022. *Computer Vision: Algorithms and Applications*, second ed. Springer.
- Thornton, E.B., Guza, R.T., 1982. Energy saturation and phase speeds measured on a natural beach. *J. Geophys. Res.* 87 (C12), 9499. <http://dx.doi.org/10.1029/JC087iC12p09499>, URL: <http://doi.wiley.com/10.1029/JC087iC12p09499>.
- Thuan, D.H., Almar, R., Marchesiello, P., Viet, N.T., 2019. Video Sensing of Nearshore Bathymetry Evolution with Error Estimate. *J. Mar. Sci. Eng.* 7 (7), 233. <http://dx.doi.org/10.3390/jmse7070233>, URL: <https://www.mdpi.com/2077-1312/7/7/233>.
- Tissier, M., Bonneton, P., Michallet, H., Ruessink, B.G., 2015. Infragravity-wave modulation of short-wave celerity in the surf zone. *J. Geophys. Res.: Oceans* 120 (10), 6799–6814. <http://dx.doi.org/10.1002/2015JC010708>, URL: <https://onlinelibrary.wiley.com/doi/abs/10.1002/2015JC010708>.
- Tsukada, F., Shimozone, T., Matsuba, Y., 2020. UAV-based mapping of nearshore bathymetry over broad areas. *Coast. Eng. J.* 62 (2), 285–298. <http://dx.doi.org/10.1080/21664250.2020.1747766>, URL: <https://www.tandfonline.com/doi/full/10.1080/21664250.2020.1747766>.
- USGS, 2022. Total Water Level and Coastal Change Forecast Viewer. URL: <https://coastal.er.usgs.gov/hurricanes/research/twlvviewer/>.
- Usuyama, N., 2018. Simple PyTorch implementations of U-Net/FullyConvNet (FCN) for image segmentation. GitHub, URL: <https://github.com/usuyama/pytorch-unet>.
- Vanderstraete, T., Goossens, R., Ghabour, T., 2003. Remote sensing as a tool for bathymetric mapping of coral reefs in the Red Sea (Hurgada – Egypt). *Belgeo* (3), 257–268. <http://dx.doi.org/10.4000/belgeo.16652>, URL: <http://journals.openedition.org/belgeo/16652>.
- Wengrove, M.E., Henriquez, M., de Schipper, M.A., Holman, R., Stive, M.J.F., 2013. MONITORING MORPHOLOGY OF THE SAND ENGINE LEESIDE USING Argus' cBathy. *Coast. Dyn.* 13.
- Yoo, J., Fritz, H.M., Haas, K.A., Work, P.A., Barnes, C.F., 2011. Depth Inversion in the Surf Zone with Inclusion of Wave Nonlinearity Using Video-Derived Celerity. *J. Waterw. Port Coast. Ocean Eng.* 137 (2), 95–106. [http://dx.doi.org/10.1061/\(ASCE\)WW.1943-5460.0000068](http://dx.doi.org/10.1061/(ASCE)WW.1943-5460.0000068), URL: <http://ascelibrary.org/doi/10.1061/%28ASCE%29WW.1943-5460.0000068>.
- Zuckerman, S., Anderson, S., 2018. Bathymetry and Water-Level Estimation Using X-Band Radar at a Tidal Inlet. *J. Coast. Res.* 345, 1227–1235. <http://dx.doi.org/10.2112/JCOASTRES-D-17-00182.1>, URL: <http://www.bioone.org/doi/10.2112/JCOASTRES-D-17-00182.1>.